Solid Freeform Fabrication 2017: Proceedings of the 28th Annual International Solid Freeform Fabrication Symposium – An Additive Manufacturing Conference
Reviewed Paper

BUILDING ZR-BASED METALLIC GLASS PART ON Ti-6AL-4V SUBSTRATE BY LASER-FOIL-PRINTING ADDITIVE MANUFACTURING

Yingqi Li, Yiyu Shen, Ming C. Leu, and Hai-Lung Tsai

Department of Mechanical and Aerospace Engineering, Missouri University of Science and Technology, Rolla, MO 65409

Abstract

Through using Zr intermediate layers, $Zr_{52.5}Ti_5Al_{10}Ni_{14.6}Cu_{17.9}$ metallic glass (MG) parts are successfully built on Ti-6Al-4V substrate by laser-foil-printing (LFP) additive manufacturing technology in which MG foils are laser welded layer-by-layer onto the substrate. The printed MG part is free of porosity, cracking and crystallization, and its properties are very similar to the original MG material. The Zr intermediate layers are aimed at preventing direct interaction between the first layer of MG foil and the Ti substrate; otherwise, the welded MG foils would peel off from the substrate due to the formation of brittle intermetallic compounds. With the use of Zr intermediate layers, the bonding strength of the printed MG part and the Ti substrate can reach 758 MPa owing to the formation of α-Zr phase.

Keywords: Metallic glass; Titanium; Laser welding; Embrittlement; Additive manufacturing.

Introduction

The amorphous atomic structure and concomitant lack of grain boundaries or slip planes endow metallic glasses (MGs), i.e., amorphous alloys, with many superior properties, such as high strength, corrosion resistance, wear resistance, etc., compared with conventional crystalline metals [1-3]. However, current applications of MGs are limited by small dimensions and simple geometries (rod, foil, thin plate, etc.) because fast cooling is necessary to produce fully amorphous structures [2].

Laser-based additive manufacturing (AM) technology is a promising method to fabricate large and complex MG parts owing to the very high heating and cooling rates of laser processing. Recently, a variety of three-dimensional MG parts were successfully built without crystallization using a newly developed laser-foil-printing (LFP) AM technology [4]. In this technology, MG foils are laser welded layer-by-layer upon the substrate to produce MG parts. Since metal foils, instead of powders, are used as feedstock, the LFP technology shows its unique advantages over powder-based AM methods on the fabrication of MG structures, such as easy to fabricate full-density part, higher cooling rate at the same laser processing condition, etc. The LFP technology can expand MG products to 3D freeform geometries with large dimensions.

Normally, a large, thick metal plate is used as the foundation substrate in LFP technology upon which additional materials are gradually added layer-by-layer. Since it is difficult or even impossible to obtain large, thick as-cast MG plates, conventional crystalline metals have to be used

as substrates. Thus, a good bonding between the MG foil and the crystalline substrate is crucial to the success of MG structures manufactured by LFP; otherwise, the welded MG foils would peel off from the substrate before the desired structure has been built because of the accumulation of residual stresses.

Many engineering applications require structures or parts with different properties in different locations. For example, a structure may need corrosion or wear resistance in one area while needs high toughness in another area. Besides properties, cost of the structure may also need to be taken into consideration. But rarely a single material can meet all these requirements. The LFP technology provides unique opportunity for printing a structure consisting of multiple materials. Theoretically, any metal which can be laser welded is a candidate material for LFP. Resultant property changes may be obtained through welding various metal foils at different desired layers or locations during LFP to meet various application needs. MG has superior corrosion resistance and wear resistance, but its intrinsic fracture toughness is usually insufficient to allow structures entirely made of MGs to obtain optimum performance [5]. In addition, to date many commercially available MGs are made from expensive metals with high-purity, e.g., high-purity Zr, resulting in very costly MGs. These factors also limit MGs' application. In many applications, there is no need to fabricate an entire MG structure; instead, most portions of the structure may be printed using cost-competitive conventional metals with favorable toughness, and only components that need to serve in extreme environment (e.g., corrosive, wear) are printed with MG. The ability to print MG parts on conventional crystalline metals, e.g. titanium alloys, stainless steels, etc., would extend the engineering applications of MG, and offer more flexibility in structure design and performance.

Laser welding of MG to crystalline metals is therefore required, but is very challenging due to the large differences in physical and chemical properties which may be present between them. Laser welding of MG to the same MG has been studied in butt-joint or bead-on-plate form [6-9]. However, there is little or no publication on laser welding of MG to crystalline metals. In this study, $Zr_{52.5}Ti_5Al_{10}Ni_{14.6}Cu_{17.9}$ MG parts were built on Ti-6Al-4V (Ti64) substrates. Our previous results show that the welded Zr-based MG foils would peel off from the Ti64 substrate when directly building an MG part on a Ti64 substrate due to the formation of hard and brittle intermetallics [10]. A feasible way to reduce the brittleness of the dissimilar bonding is to use an intermediate layer to separate the two dissimilar materials. The intermediate layer should be highly soluble with both materials. Zr has similar chemical properties to Ti, and Ti-Zr system can form hcp solid solution over the complete composition range [11]. On the other hand, Zr is the main element of the selected MG, and Zr-based MG parts can be built on Zr substrates by LFP without peeling off due to the formation of α-Zr phase in the MG-Zr interface [10]. Thus, pure Zr foil was chosen as the intermediate layer to improve the bond between Zr-based MG part and Ti64 substrate in this study. The properties of the printed MG part will be discussed first, and then this paper will focus on the study of the dissimilar bonding between the MG part and the Ti64 substrate.

Experimental

Since this paper focuses on the bonding between Ti64 alloy and MG, 12-mm-thick Ti64 plates, instead of 3D printed Ti64 parts, were used as the substrates in this experiment to shorten the fabrication time. The thickness of a layer of MG foil with nominal chemical composition of

$Zr_{52.5}Ti_5Al_{10}Ni_{14.6}Cu_{17.9}$ (at. %) (Liquidmetal®, LM105) was approximately 200 μm. 200-μm-thick pure Zr foil (Zr 702) was used as the intermediate layer. Before laser processing, the substrates and foils were slightly grinded using abrasive papers to remove surface oxides, and then cleaned using ethanol.

The LFP system developed at the Laser-Based Manufacturing Lab, Missouri S&T, schematically shown in Fig. 1, was used in this experiment. This system mainly consists of two lasers: a continuous wave fiber laser (IPG YLP-1000) with 1070 nm wavelength for foil-welding and a pulsed UV laser (Coherent AVIA-355X) with 355 nm wavelength and 30 ns pulse duration for foil-cutting. In this study, the welding laser beam entered a scanner (SCANLAB) and then was focused on the foil surface, and the beam diameter (*D*) at the focus was about 170 μm. The substrate was mounted on a computer controlled three-axis motion stage (Aerotech). A layer of foil was placed and fixed on the substrate via laser spot welding using a mold-plate with a predetermined hole-pattern (see Fig. 2(a)). Then, the scanner scanned multi-passes to weld the foil onto the substrate, as shown in Fig. 2(b) and (d). After the welding process was done, the motion stage shifted the workpiece to the location under the UV laser and the foil was cut by the UV laser along the contour of the welded region to remove the redundant foil (see Fig. 2(c)). Another layer of fresh foil was placed on the top of the workpiece for the process of next layer. The above processes were repeated until the desired part was built. All samples were processed inside a chamber with Ar shielding gas flow.

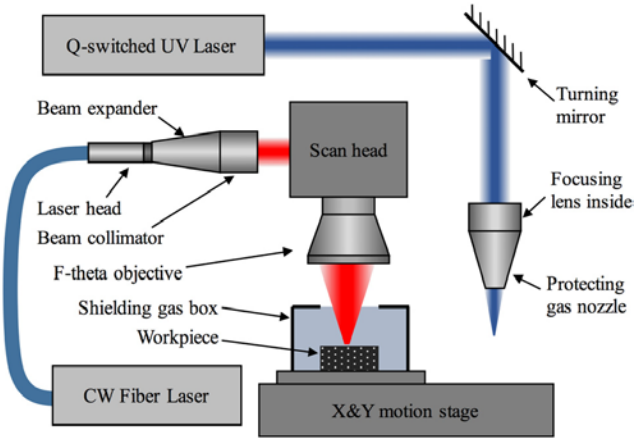

Figure 1 The LFP system developed at the Laser-Based Manufacturing Lab, Missouri S&T. Reprinted from Ref. [12].

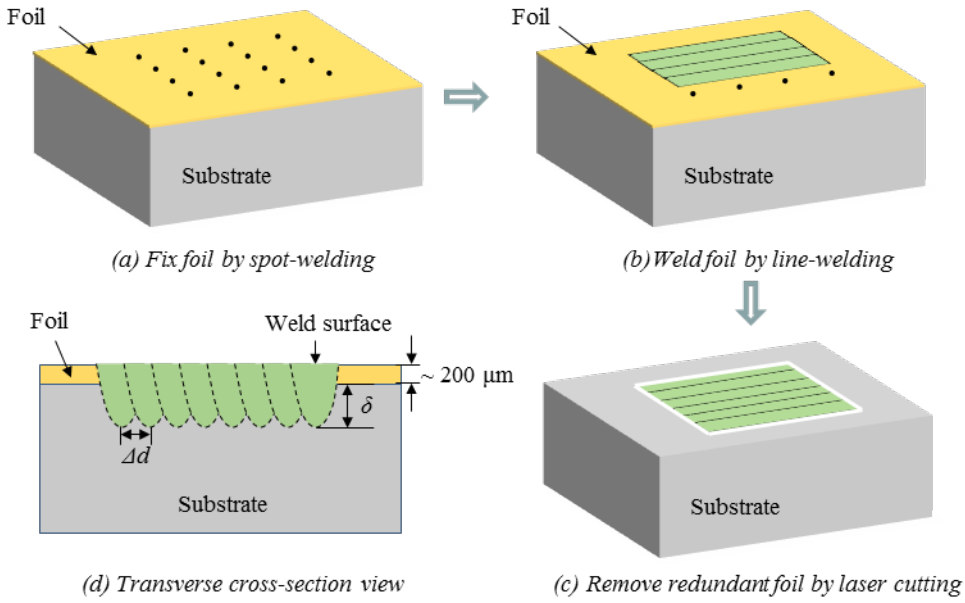

Figure 2 (a-c) Schematic of the LFP process; (d) schematic view of the transverse cross-section after the first layer of foil is welded onto the substrate. Δd is the hatch space, and δ indicates the penetration. Reprinted from Ref. [10].

Two cases were compared in this paper, i.e., without any intermediate layer (Case 1) and with Zr intermediate layers (Case 2). For Case 1, MG foils were directly welded onto the Ti64 substrate, and only ten layers of MG foil were welded since the welded foils peeled off from the substrate before the desired part was built. For Case 2, the first and second layers were both Zr foils. After that, 25 layers of MG foil were further welded onto the workpiece to construct a 5-mm-thick MG part with a base area of 15 mm× 20 mm (see Fig. 3). To reduce heat accumulation, the time lapse between two adjacent scan passes was 10 s. The used laser power (P), laser scanning speed (v) and hatch space (Δd) for each layer of welding are listed in Table 1. The used P and v values were selected after parametric study to ensure continuous and stable welding passes and small penetration depth at the same time.

Table 1 Parameters for each layer of welding

Layer	**Laser power (P) (W)**	**Laser scanning speed (v) (mm/s)**	**Hatch space (Δd) (mm)**
1st layer of Zr foil (if any)	500	500	0.12
2nd layer of Zr foil (if any）	500	450	0.12
1st layer of MG foil	500	570	0.12
2nd-25th layer of MG foil	500	650	0.14

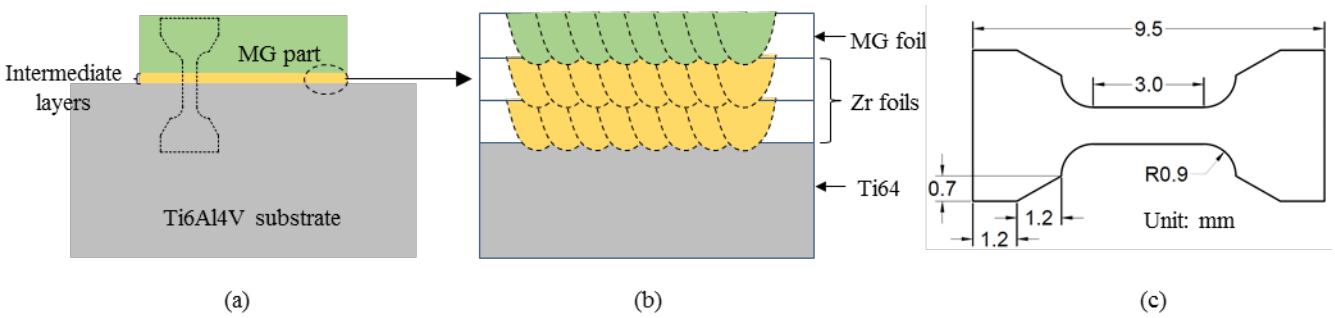

Figure 3 (a) Schematic of the printed MG part built on Ti64 substrate with intermediate layers; (b) schematic of the bonding between MG and Ti64 when using two layers of Zr foil as intermediate layers; (c) dimensions of the miniature tensile test specimen.

After the MG part was built, miniature tensile test specimens were cut from the substrate and the printed MG part by wire electric discharge machining (EDM), to test the bonding strength between the Ti64 substrate and the MG part, as schematically shown in Fig. 3(a). The dimensions of the miniature tensile test specimens are shown in Fig. 3(c), and the thickness was 1 mm. The tensile test was conducted on an INSTRON-5969 testing machine. Five specimens were tested, and the mean value was reported. The tensile strength of the printed MG part was also tested using the same method. The microstructure and chemical composition were analyzed using X-ray diffraction (XRD), optical microscope (OM), and scanning electron microscope (SEM) equipped with energy dispersive spectroscopy (EDS). The glass transition temperature and crystallization temperature of the MG part were measured by differential scanning calorimeter (DSC). The metallographic specimens for OM and SEM analysis were prepared following the general procedure of metallurgical sample preparation.

Results and Discussion

Figure 4(a) shows the OM image of the transverse (perpendicular to the laser scanning direction) cross-section of the printed MG part. This cross-section was etched using a solution of 100 ml H_2O, 2 ml H_2O_2 and 0.1 ml HF which can reveal the crystallization of LM105 MG occurred during laser scanning [4]. It can be seen that the cross-section is featureless; porosity, cracking and crystallization were not observed. The XRD result of the printed MG part, which was conducted on the longitudinal (parallel with the laser scanning direction) cross-section of the middle plane, also confirms that the printed MG part is fully amorphous within the detection limit of XRD (~ 7% [13]) (see Fig. 4(b)). DSC was used to compare the glass transition temperature (T_g) and crystallization temperature (T_x) of the printed MG part and the original MG at a heating rate of 20 °C/min, and the results are shown in Fig. 4(c). For the printed MG part, $T_g \approx 397$ °C, $T_{x1} \approx 475$ °C and $T_{x2} \approx 482$ °C. These values are very close to those of the original MG, in which $T_g \approx 394$ °C, $T_{x1} \approx 470$ °C and $T_{x2} \approx 478$ °C. Tensile tests were conducted to investigate the mechanical properties of the printed MG part. For comparison, the original LM105 MG with a thickness of 750 μm was also tested. The tensile test was conducted along the laser scanning direction, and four samples were tested and the average value was reported. The original MG has a yield strength of ~ 862 MPa and an ultimate strength of ~ 1533 MPa with an elongation-to-failure of ~ 5.8%. The printed MG part exhibits higher yield strength (~ 1138 MPa) and ultimate strength

(~ 1758 MPa), but slightly lower elongation-to-failure (~ 4.9%). The above observations show that the printed MG part is extremely similar to the original MG.

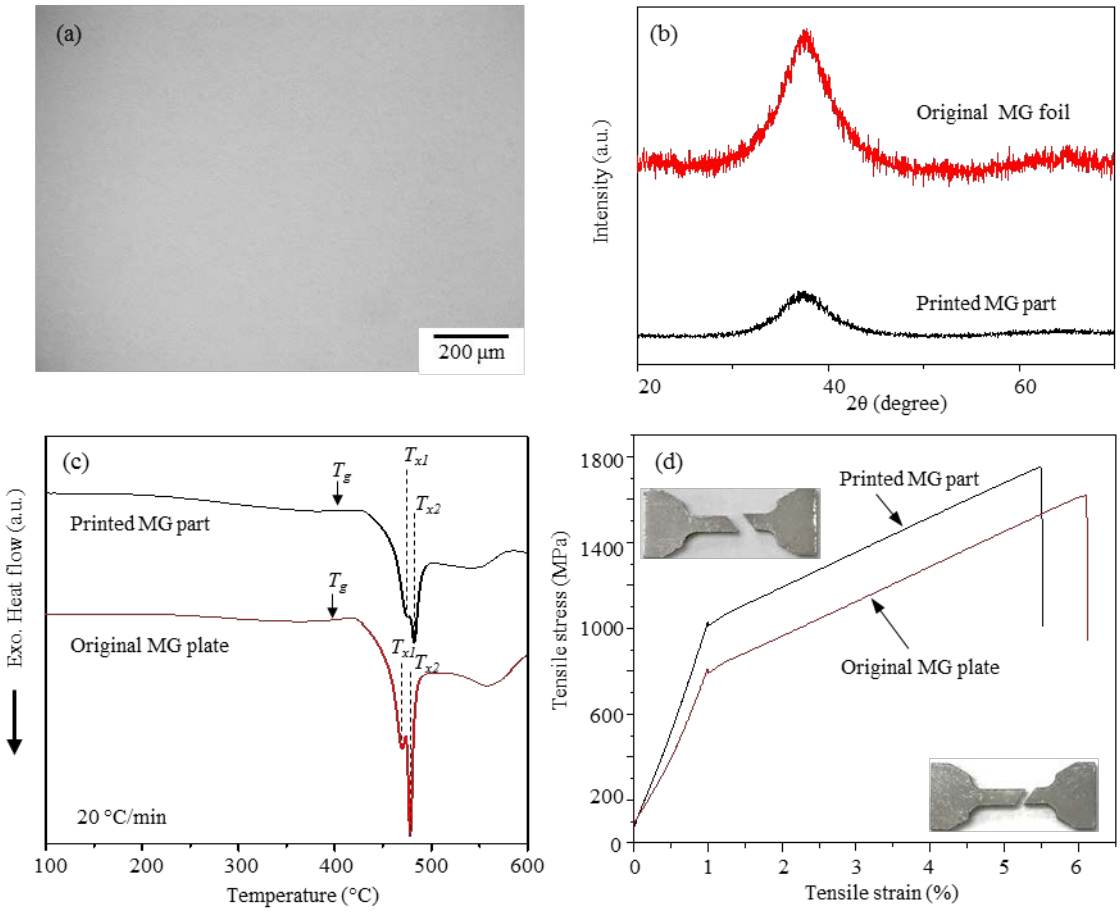

Figure 4 The printed MG part: (a) OM image of the transvers cross-section; (b) XRD pattern conducted on the longitudinal cross-section of the middle plane; (c) DSC profile; (d) tensile stress-strain curve. For comparison, the data for the original MG were also included.

Figure 5 shows the bonding area between the MG part and the Ti64 substrate without intermediate layer (subfigure (a)), or with Zr intermediate layers (subfigure (b)). When an MG part was directly built on the Ti64 substrate, the welded MG foils completely peeled off from the substrate after 10 layers of MG foil were welded, indicating a weak bonding between the MG and the Ti64, as shown in Fig. 5(a). On the contrary, when Zr intermediate layers were used, the sample did not fracture during the part fabrication (see Fig. 5(b)). Tensile test was then performed on the joints with intermediate layers to measure the bonding strength between the MG part and the Ti64 substrate. The stress-strain curve is shown in Fig. 6(a). The average bonding strength between the MG part and the Ti64 substrate is about 758.5 MPa. The tensile test specimens fractured at the interface between the first layer of Zr foil and the Ti64 substrate, as shown in Fig. 6(b). The tested bonding strength is 20% less than the ultimate tensile strength (UTS) of Ti64 alloy (~950 MPa), but is 62% higher than the UTS of Zr 702 (~468 MPa). However, the specimen shows nearly no plastic deformation prior to failure (with an elongation to fracture of only ~ 0.5%), indicating a brittle fracture.

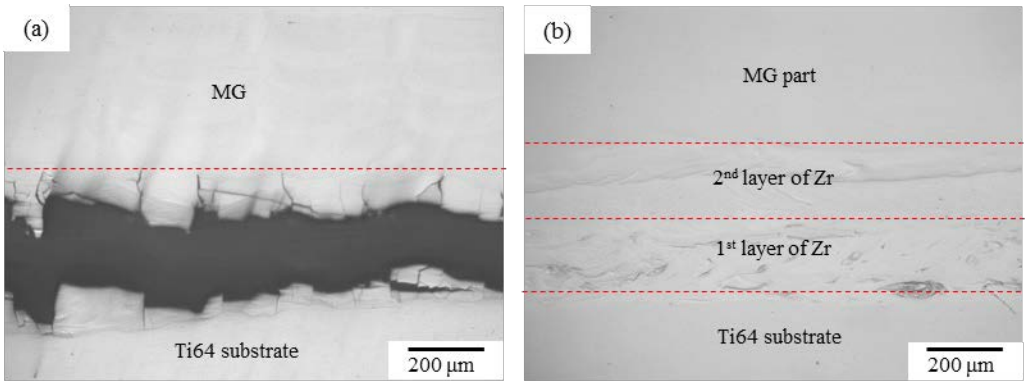

Figure 5 The bonding between the MG part and the Ti64 substrate: (a) without intermediate layer; (b) with Zr intermediate layers.

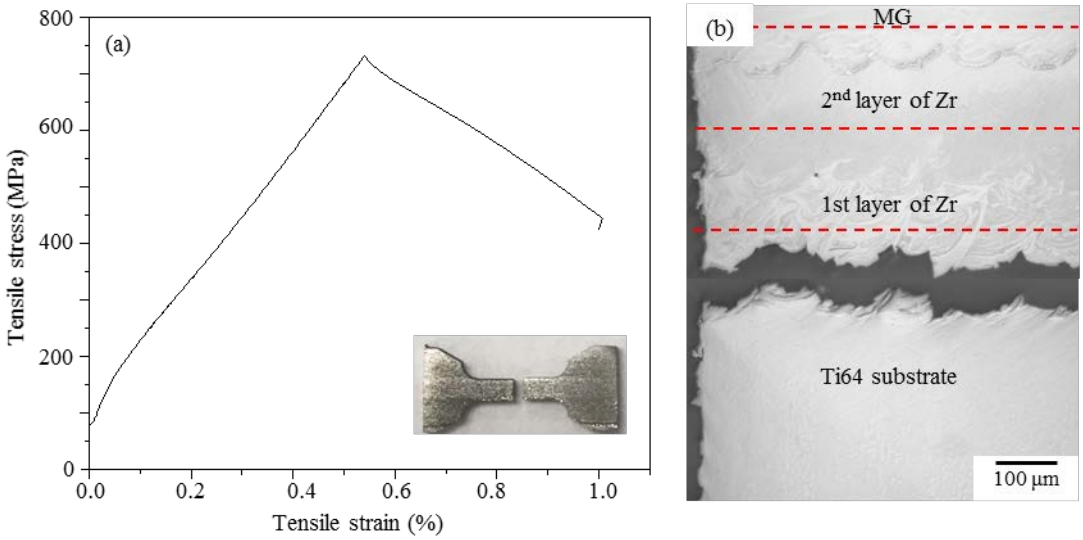

Figure 6 (a) Tensile strain-stress curve of the bonding between the MG part and the Ti64 substrate with Zr intermediate layers; (b) OM image showing the fracture position of the tensile test specimen.

The chemical composition and microstructure were then analyzed and compared on the bonding area between the first layer of MG foil and the Ti64 substrate for these two cases. A layer of MG foil was first directly welded onto the Ti64 substrate without any intermediate layer at P = 500 W, v = 580 mm/s, Δd = 0.25 mm. Figure 7(a) is the backscattered electron image of the transverse cross-section of the bonding area. It can be seen that the welding is a keyhole-mode, instead of conduction-mode, which is consistent with the calculated laser intensity $I = P/(\pi D^2/4) = 2.2\times10^6$ W/cm^2. The depth of penetration (δ) is about 95 μm. In addition, the transverse cross-section shows a swirling structure, especially at the bottom of the welding metal, i.e., the penetration area or the MG-Ti interface. Note the interface refers to the penetration area in this paper. This swirling structure indicates the incomplete mixing between the melted Ti64 substrate and the MG foil due to rapid solidification in laser welding. Figure 7(b) shows the longitudinal cross-section of the bonding area, from which cracking can be easily observed at the MG-Ti interface.

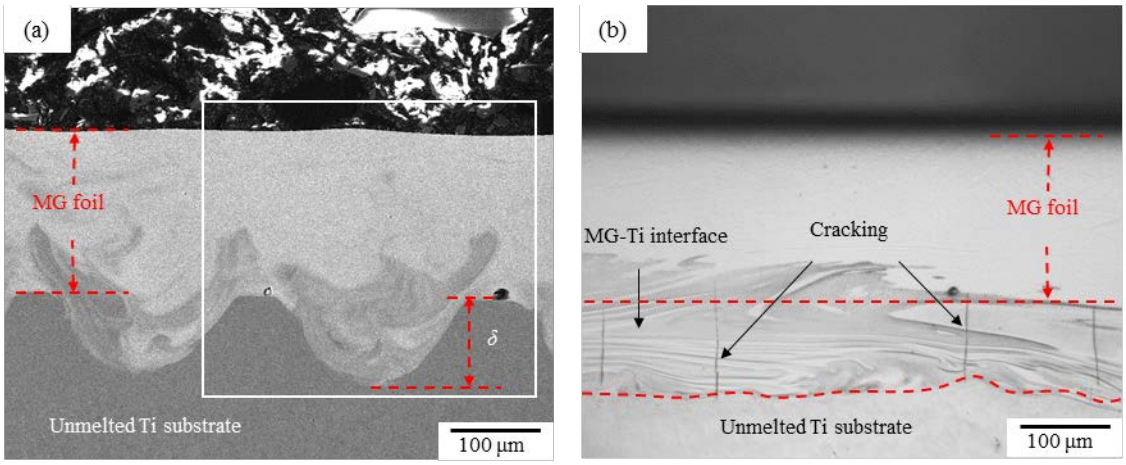

Figure 7 The bonding between the first layer of MG foil and the Ti64 substrate without intermediate layer: (a) backscattered electron image of the transverse cross-section; (b) OM image of the longitudinal cross-section.

Figure 8 shows the distribution of the major elements (Zr and Ti) in the MG-Ti bonding corresponding to the rectanglular area in Fig. 7(a). Table 2 summarizes the chemical composition of the tested points in Fig. 8. It can be seen that the MG-Ti interface, which has highest cracking susceptibiliy, is a Ti-rich area that has higher Ti content and less Zr than the MG foil (see Fig. 8 and Table 2). In addition, the distribution of Ti is not uniform in the penentration area (see Fig. 8(c) and (d)), which is consistent with the swirling structure shown in Fig. 7. An addition of 2-5 at. % of Ti can improve the glass forming ability of Zr-Cu-Ni-Al amorphous alloys; however, for higher Ti content ($\geq$ 10 at. %) and lower contents of Cu, Ni and Al (Cu + Ni + Al $\leq$ 35 at. %), the glass forming ability decreases and, in turn, the formation of crystalline is promoted [14]. In most of the penetration area, the Ti content is larger than 50 at. %, and Cu + Ni + Al $\leq$ 35 at. %, e.g., points 1-4 (see Table 2). Thus, the formation of crystalline phases is promoted. There are at least six elements (Zr, Ti, Al, Ni, Cu, and V) existing in the penetration area, and these elements are not all mutually soluble [15], which would increase the possibility of forming a large amount of intermetallic compounds. The XRD pattern, tested at the MG-Ti interface after removing the MG by mechanical grinding, shows that the microstructure is a blend of amorphous phase and intermetallics (could be $ZrCu_2$, Ni_2Ti, Ni_2Zr_3, Al_2Zr), as shown in Fig. 9. Intermetallics are often hard and brittle, their formation may be responsible for the high cracking susceptibility in the penetration area [16]. On the other hand, the large difference in coefficient of thermal expansion (CTE) between LM105 MG (12.0 μm/m-°C) and Ti64 (8.6 μm/m-°C) would result in large residual stresses, which might promote the formation of cracking in the area with high cracking susceptibility.

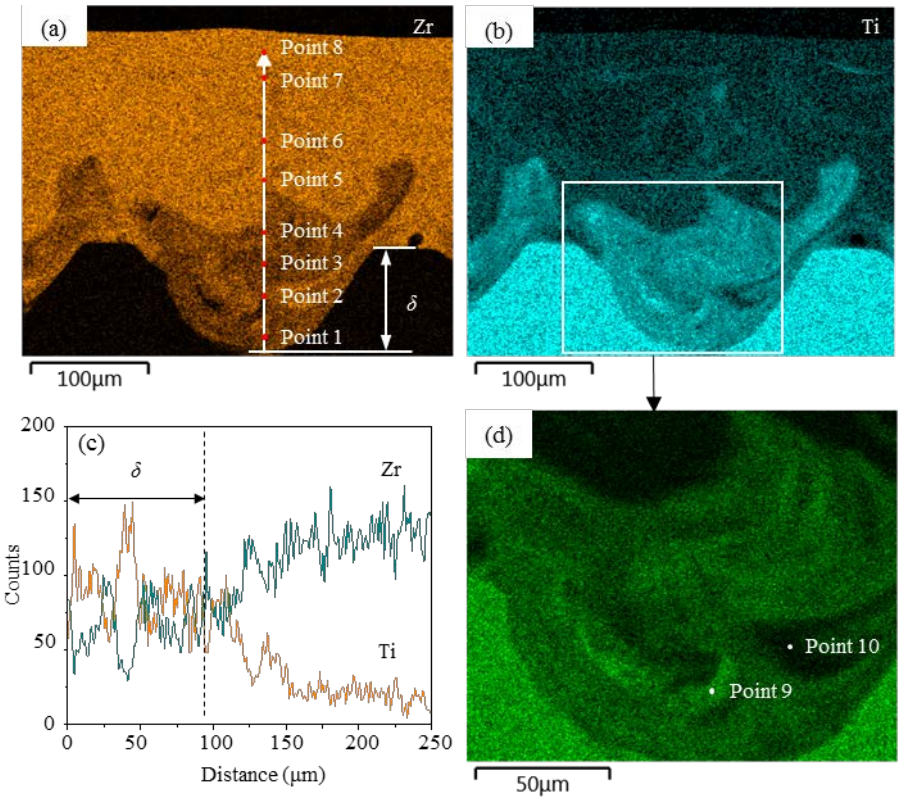

Figure 8 (a) and (b) Element maps of Zr and Ti corresponding to the rectangular area in Fig. 7(a); (c) element distribution along the white arrow in (a); (d) magnified element map of Ti. Only the major elements are shown here.

Table 2 EDS point analysis for Fig. 8 (at. %).

Element		**Zr**	**Ti**	**Al**	**Ni**	**Cu**	**V**
Original MG	Nominal	52.5	5	10	14.6	17.9	-
	EDS calculated	48.25	5.50	9.55	15.05	21.65	-
Point 1		23.00	50.33	10.29	5.0	8.61	2.73
Point 2		20.34	50.74	10.17	6.64	9.37	2.75
Point 3		14.00	61.54	10.19	4.22	6.91	3.15
Point 4		18.94	55.16	9.81	5.43	8.11	2.55
Point 5		36.89	23.99	9.72	11.28	16.25	1.09
Point 6		42.58	16.12	9.62	13.30	18.38	-
Point 7		48.55	7.09	9.45	13.82	21.09	-
Point 8		48.87	6.57	9.09	13.83	21.64	-
Point 9		7.37	72.90	10.55	2.42	3.25	3.51
Point 10		44.59	13.61	9.78	12.78	19.24	-

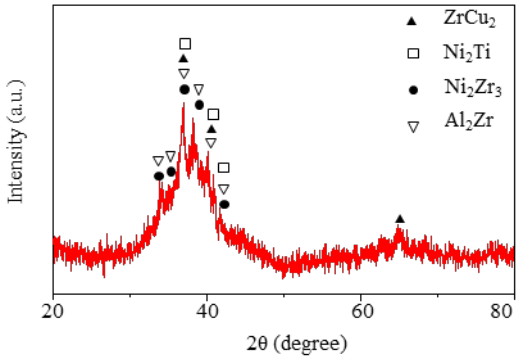

Figure 9 XRD pattern taken at the MG-Ti interface.

Figure 10 shows the transverse and longitudinal cross-sections of the bonding area between the first layer of MG foil and the Ti64 substrate with Zr intermediate layers. The penetration depths δ_1 for welding the first layer of Zr, δ_2 for welding the second layer of Zr, and δ_3 for welding the first layer of MG are around 67 μm, 115 μm, and 84 μm, respectively, as shown in Fig. 10(a). This bonding consists of three interfaces, i.e., Zr-Ti interface, Zr-Zr interface and MG-Zr interface (see Fig. 10(b)). Unlike the case without intermediate layer, cracking was not observed in these three interfaces from the cross-sections.

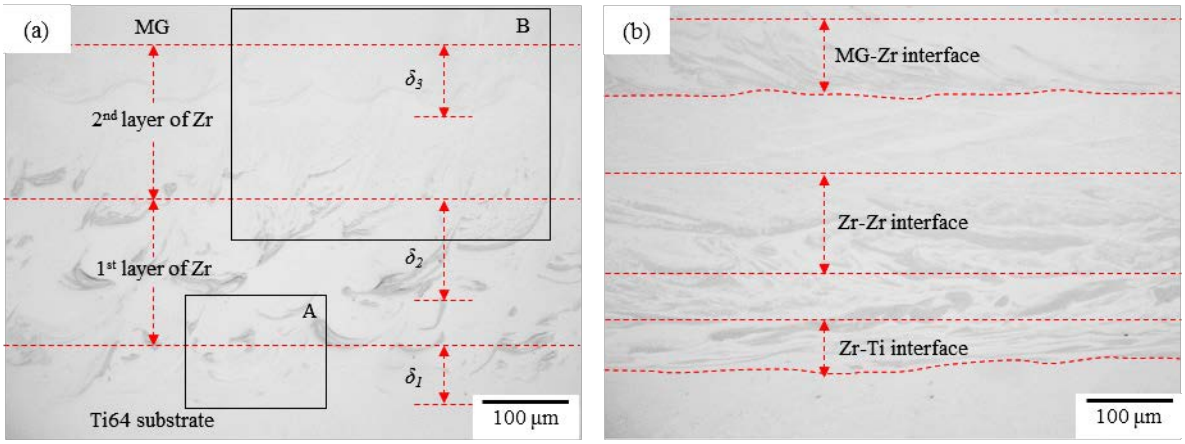

Figure 10 The bonding between the first layer of MG foil and the Ti64 substrate with Zr intermediate layers: (a) OM image of the transverse cross-section; (b) OM image of the longitudinal cross-section.

Figure 11 shows the element distribution at the bottom of the first layer of Zr foil corresponding to the area "A" in Fig. 10(a). The chemical composition of the tested points on Fig. 11 is listed in Table 3. It can be seen that the chemical composition distribution of the intermediate layer is not very uniform, caused by incomplete mixing between the melted Ti64 substrate and Zr foil, as shown in Fig. 11(a) and (b). Generally, there is ~30 at. % of Ti mixed with Zr in the intermediate layer (Fig. 11(c)), e.g., points 2-4. Figure 12 shows the chemical composition distribution at the MG-Zr interface, corresponding to the area B in Fig. 10(a). The chemical composition of the tested points in Fig. 12 is also shown in Table 3. For the second layer of Zr, the distribution of chemical composition fluctuates in the area close to the first layer of Zr, and becomes relatively uniform in the area close to the MG, as shown in Fig. 12(b) and (d). Additionally, there are ~10 at. % of Ti

and ~ 90 at. % of Zr in the area with uniform chemistry distribution, e.g., points 6-8 (see Table 3). With the use of Zr intermediate layers, at the bottom of the first layer of MG foil, the content of Ti is significantly reduced, and meanwhile the increase of Zr content is considerable, as shown in Fig. 12, compared with the case without intermediate layer (Fig. 8). For example, points 9-11 in Fig. 12(a) have ~10 at. % of Ti and ~70-80 at. % of Zr (see Table 3); however, points 1-4 in Fig. 8(a) have ~50-60 at. % of Ti and ~14-23 at. % of Zr.

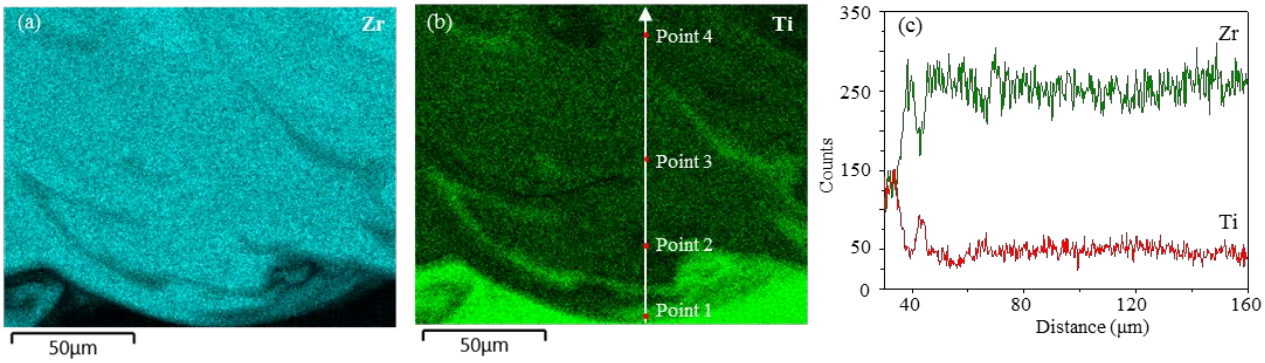

Figure 11 (a) and (b) Element maps of Zr and Ti in the first layer of Zr foil corresponding to the area A in Fig. 10(a); (c) element distribution along the white arrow in (b). Only major elements are shown here.

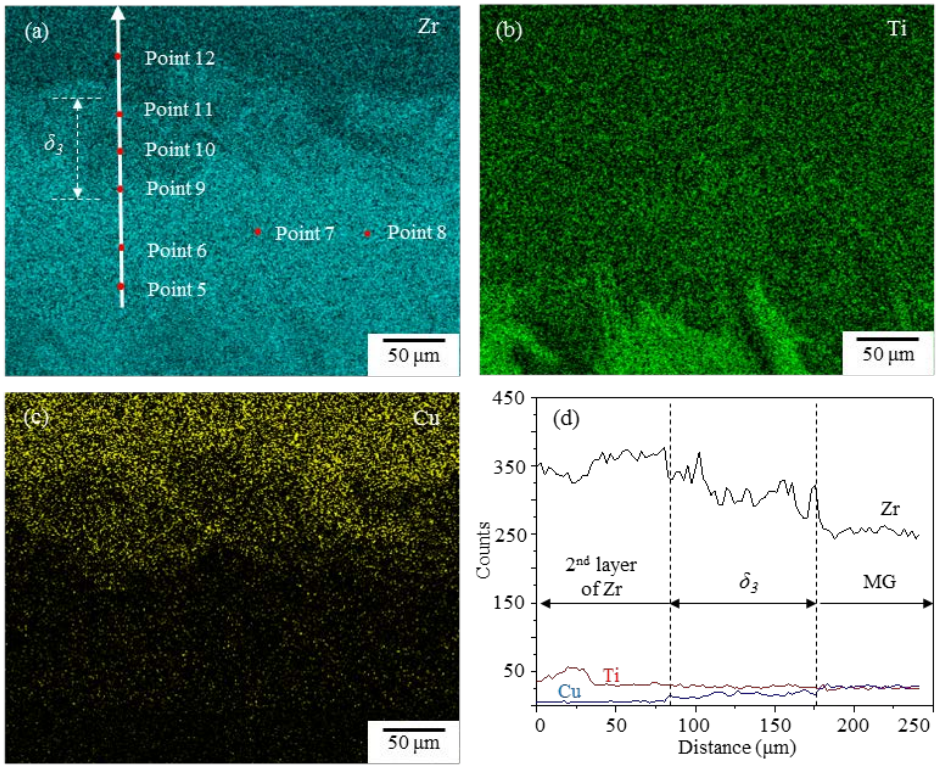

Figure 12 (a-c) Element maps of Zr, Ti, and Cu at the MG-Zr interface, corresponding to the area B in Fig. 10(a); (d) element distribution along the white arrow in (a). Only major elements are shown here.

Table 3 Point chemical composition for Figs. 11 and 12 (at. %).

Element		Zr	Ti	Al	Ni	Cu	V
Original MG	Nominal	52.5	5	10	14.6	17.9	-
	EDS calculated	48.25	5.50	9.55	15.05	21.65	-
Point 1		25.36	63.22	3.71	-	-	3.71
Point 2		68.50	27.24	2.62	-	-	1.64
Point 3		64.29	30.31	3.47	-	-	1.92
Point 4		68.28	27.62	2.66	-	-	1.43
Point 5		84.38	15.62	-	-	-	-
Point 6		86.99	11.35	1.66	-	-	-
Point 7		90.6	9.4	-	-	-	-
Point 8		89.88	10.12	-	-	-	-
Point 9		78.71	10.06	3.32	3.99	3.92	-
Point 10		69.32	9.13	5.14	7.99	8.42	-
Point 11		71.99	9.60	4.40	6.63	7.38	-
Point 12		53.57	7.09	8.03	15.34	15.98	-

Figure 13 shows the XRD patterns obtained at the MG-Zr interface after removing the MG, at the Zr-Zr interface after removing the second layer of Zr, and at the Zr-Ti interface after removing the first layer of Zr by mechanical grinding. For comparison, the XRD pattern of the original Zr foil is also included. We can see that the microstructures at the Zr-Ti interface and at the Zr-Ti interface both are α-Zr solid solutions. However, because the solute elements and their percentages that are incorporated in the hcp crystalline lattice of α-Zr are different for the Zr-Ti and Zr-Zr interfaces, their XRD patterns are not completely the same. For the Zr-Ti interface, the solute elements are Ti, Al, and V, but the solute is mainly Ti for the Zr-Zr interface (Table 3). In addition, the solute content is higher at the Zr-Ti interface than that at the Zr-Zr interface. Thus, the peak shift and broadening of the XRD pattern is more evident for the Zr-Ti interface (see Fig. 13). For the MG-Zr interface, because of the very high content of Zr (see Fig. 12 and Table 3), α-Zr phase formed. In addition, amorphous phase and ZrCu intermetallic are also detected. Because of the very low content of Cu at the MG-Zr interface (Table 3), the formation of ZrCu would not considerably contribute to the brittleness of the weldment. Compared with the intermetallics formed at the bonding between the MG and Ti64 without intermediate layer, α-Zr phase is more soft and ductile. Therefore, the improved bonding strength between the MG and Ti64 with Zr intermediate layers seems to be contributed by the very high Zr content and the resultant formation of α-Zr phase.

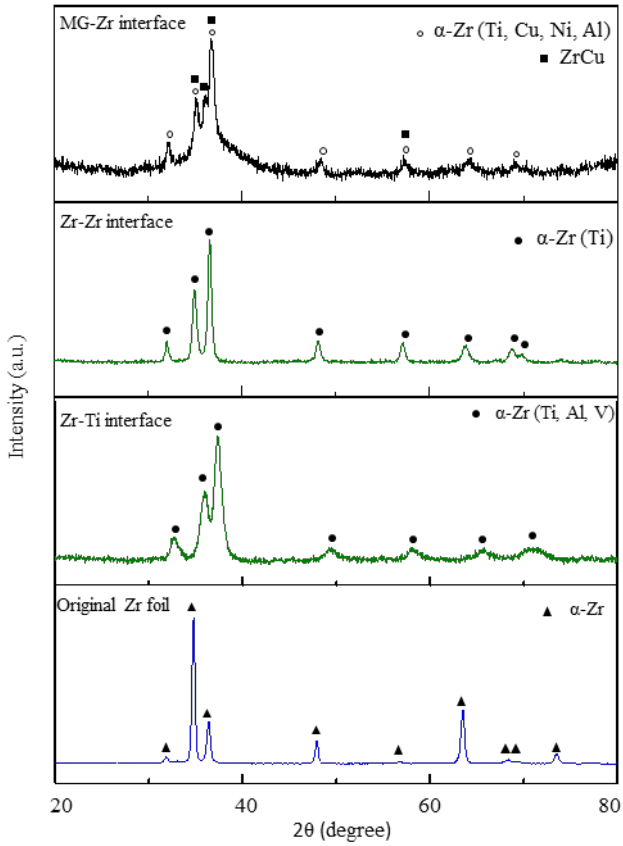

Figure 13 XRD patterns obtained at the MG-Zr interface, Zr-Zr interface and Zr-Ti interface.

Conclusions

$Zr_{52.5}Ti_5Al_{10}Ni_{14.6}Cu_{17.9}$ metallic glass parts were successfully built upon Ti64 substrates by laser-foil-printing (LFP) additive manufacturing in this paper. Pores, cracking and crystallization were not observed in the printed MG part, and its glass transition temperature, crystallization temperature, and tensile strength are nearly the same as the original MG material. When directly building a MG part on the Ti64 substrate, the welded MG foil peeled off from the substrate due to the formation of brittle intermetallic compounds at the MG-Ti interface caused by excessive mixing of the melted Ti substrate with the MG. When Zr intermediate layers were used, the Ti64 and the MG part had a bonding strength of ~758 MPa, and the tensile test specimen fractured at the Zr-Ti interface. This improved bonding is contributed by the very high Zr content and the resultant formation of α-Zr phase in the dissimilar bonding.

Acknowledgements

This work was supported by the Department of Energy (grant number DE-FE0012272); the University of Missouri System (award number FastTrack-16002R).

References

[1] J. Schroers, Processing of bulk metallic glass, Adv. Mater. 22 (2010) 1566-1597.

[2] W. H. Wang, C. Dong, C. H. Shek, Bulk metallic glasses, Mater. Sci. Eng. R 44 (2004) 45-89.

[3] A. Inoue, Bulk amorphous and nanocrystalline alloys with high functional properties, Mater. Sci. Eng. A 304-306 (2001) 1-10.

[4] Y. Shen, Y. Li, C. Chen, H.-L. Tsai, 3D printing of large, complex metallic glass structures, Mater. Des. 117 (2017) 213-222.

[5] W. L. Johnson, J. Plummer, Is metallic glass poised to come of age?, Nature materials 14 (2015) 553-555.

[6] G. Wang, Y. J. Huang, M. Shagiev, J. Shen, Laser welding of $Ti_{40}Zr_{25}Ni_3Cu_{12}Be_{20}$ bulk metallic glass, Mater. Sci. Eng. A 541 (2012) 33-37.

[7] H. S. Wang, H. G. Chen, J. S. C. Jang, M. S. Chiou, Combination of a Nd:YAG laser and a liquid cooling device to $(Zr_{53}Cu_{30}Ni_9Al_8)Si_{0.5}$ bulk metallic glass welding, Mater. Sci. Eng. A 528 (2010) 338-341.

[8] N. H. Tariq, B. A. Hasan, J. I. Akhter, Evolution of microstructure in $Zr_{55}Cu_{30}Al_{10}Ni_5$ bulk amorphous alloy by high power pulsed Nd:YAG laser, J. Alloy. Compd. 485 (2009) 212-214.

[9] B. Li, Z. Y. Li, J. G. Xiong, L. Xing, D. Wang, Y. Li, Laser welding of $Zr_{45}Cu_{48}Al_7$ bulk glassy alloy, J. Alloy. Compd. 413 (2006) 118-121.

[10] Y. Li, Y. Shen, C. Chen, M. C. Leu, H. L. Tsai, Building metallic glass structures on crystalline metal substrates by laser-foil-printing additive manufacturing, J. Mater. Process. Technol. 248 (2017) 249-261.

[11] S. M. Equo Kobayashi, Hisashi Doi, Takayuki Yoneyama, Hitoshi Hamanaka, Mechanical properties of the binary titanium-zirconium alloys and their potential for biomedical materials, Journal of Biomedical Materials Research 29 (1995) 943-950.

[12] C. Chen, Y. Shen, H. L. Tsai, A Foil-Based Additive Manufacturing Technology for Metal Parts, ASME J. Manuf. Sci. Eng. 139 (2016) 024501.

[13] P. L. Michael Miller, Bulk Metallic Glasses, 2008.

[14] U. Kühn, J. Eckert, N. Mattern, L. Schultz, ZrNbCuNiAl bulk metallic glass matrix composites containing dendritic bcc phase precipitates, Applied Physics Letters 80 (2002) 2478-2480.

[15] T. Massalski, H. Okamoto, P. Subramanian, L. Kacprzak, Binary alloy phase diagrams, ASM, 1986.

[16] Z. Sun, ION, J. C. , Laser welding of dissimilar metal combinations, J. Mater. Sci. 30 (1995) 4205-4214.